Magneto-Rheological Variable Stiffness and Damping Torsional Vibration Control of Powertrain System

Xiaomin Dong*, Wenfeng Li, Jianqiang Yu, Chengwang Pan, Jun Xi, Yaqin Zhou and Xuhong Wang

State Key Laboratory of Mechanic Transmission, Chongqing University, Chongqing, China

A novel magneto-rheological variable stiffness and damping torsional vibration absorber (MR-VSDTVB) is proposed, fabricated and tested. According to the test data, the control model of MR-VSDTVB is established. Meanwhile, the analysis of the multi-degree-of-freedom model of the powertrain system provides the key frequency and the rotating velocity of the torsional vibration control of the powertrain system and further determines the installation position and structural parameters of MR-VSDTVB. Besides, a human-simulated intelligent controller (HSIC) is developed and numerical simulation of the powertrain system with MR-VSDTVB is carried out. Ultimately, the results verify the effectiveness of the powertrain system with MR-VSDTVB and the semi-active HSIC algorithm on the torsional vibration control.

Keywords: MR-VSDTVB, powertrain system, semi-active, HSIC, control model

INTRODUCTION

With the gradual improvement of people's ride comfort requirements, the research of vehicle noise, vibration, and harshness (NVH) characteristics has become a hot spot. Many factors would affect the NVH performance of vehicles, among which the torsional vibration of the powertrain system is absolutely critical (Qing-Hua et al., 2015). The power of the vehicle is generated periodically in every second rotation of crankshaft for each cylinder creating dynamic forces on the crankshaft. The torque generated by the engine is the main reason for the torsional vibration of the automobile power system (Ye, 2012). As the torsional vibration energy of powertrain system is transmitted to the vehicle body, the vehicle will produce vibration and noise, which will ultimately affect the ride comfort.

In addition to improving and optimizing the control system of electronic fuel injection (EFI) engines, the most common method of suppressing torsional vibration is to install a torsional vibration absorber in the powertrain system. The common installation positions of the torsional vibration absorbers in the powertrain system are the engine output shaft or the specific inertia disks directly. The first type of effective torsional vibration absorber includes the dual mass flywheel (DMF), the centrifugal pendulum vibration absorber (CPVA) and the DMF with CPVA, etc. (Johann et al., 2014). The second type of torsional vibration absorber is the dynamic vibration

absorber, which is attached to the primary system. Dynamic vibration absorbers have attracted the attention of many scholars because they do not need to change the powertrain system significantly. Besides, Dynamic vibration absorbers can also effectively improve the torsional vibration response of the powertrain system in a large frequency range.

In recent years, with the emergence of various new intelligent materials, the research on semi-active dynamic vibration absorber is also prevailing. The semi-active dynamic vibration absorber can vary its inherent frequency to follow the external excitation frequency, which needs very little energy input. The frequency of dynamic vibration absorber can be changed by means of variable stiffness or variable inertia. Furthermore, the semi-active variable stiffness torsional vibration absorber becomes the most common type on account of its ease of control and simplicity of structure (Xu, 2010; Zhang, 2015). Davis et al. (1997) proposed a piezoelectric semi-active torsional vibration absorber, which controlled the stiffness of piezoelectric ceramics by changing the electric field and ultimately achieved semi-active control of the natural frequency of the absorber. Williams et al. (2002) used shape memory alloys as a variable stiffness core component and proposed a novel semi-active variable stiffness vibration absorber. Because the stiffness of the material varied with the working temperature, the working temperature could be changed by turning the power on or off. The variable stiffness characteristic of the magneto-rheological elastomer (MRE) under the external magnetic field made it applicable to the frequency-tunable absorber. A series of torsional vibration absorbers with simple structure and superior performances have been designed (Deng and Gong, 2007; Hoang, 2011; Fu et al., 2016; Qian et al., 2017; Wang and Jing, 2018; Yu et al., 2018). Nagaya et al. (1999) designed a MRE absorber and proposed a system with the MRE absorber, and then a relevant controller of the system with the MRE absorber was proposed by setting the torsional vibration amplitude of the system as the input signal and the minimum torsional vibration amplitude of the system response as the control objective. Through numerical simulation, Zhang and Li (2009) proved that the semi-active vibration absorber had a good damping effect by utilizing a real-time control strategy. Gao et al. (2018) realized the torsional vibration control of the system in a wide range of excitation frequency by configuring the MRE absorber groups in the system and using the input excitation frequency as the input signal. Huang et al. (2019), Sun et al. (2016) and Harris et al. (2017) applied MR fluid to the design of the variable stiffness and damping devices, and proved their effectiveness through prototype test.

At present, there are few studies on the application of magneto-rheological fluid in variable stiffness devices, especially torsional variable stiffness devices, and the research on variable stiffness devices mainly focuses on theoretical analysis and physical realization, which often ignores the practical limitations of the prototype, such as the range of variable stiffness values and other nonlinearities in an actual implementation.

This paper focuses on the application of MR fluid in a magneto-rheological variable stiffness and damping torsional vibration absorber (MR-VSDTVB), which is designed, fabricated and tested to demonstrate the output characteristics of MR-VSDTVB. Then, the research on the powertrain system with MR-VSDTVB is carried out. Variable stiffness and variable damping control strategy and its control performance will be investigated. The organization of this study is as follows. In Section 2, the vibration characteristics of a powertrain system are analyzed. The discussion on MR-VSDTVB is shown in Section 3. The human-simulated intelligent control (HSIC) algorithm of the powertrain system with MR-VSDTVB is investigated in Section 4. Section 5 reveals the simulation results and discussion. Conclusions are drawn in section 6.

VIBRATION CHARACTERISTICS OF THE POWERTRAIN SYSTEM

The automobile powertrain system is a typical multi-degree-of-freedom system. A front-mounted rear drive car powertrain system, which was proposed by Kang et al. (2014), etc. is adopted here. Based on the principle that the kinetic energy and potential energy of the system remain unchanged before and after simplification, the equivalent model is composed by simplifying the powertrain system as the inelastic inertia disks and the massless inertial axes, as shown in **Figure 1**. The corresponding relationship between the components of the powertrain system and the parameters in **Figure 1** is detailed in nomenclature to ensure the readability of the paper, which is not listed separately here. The red block in **Figure 1** is the proposed torsional vibration absorber with variable stiffness and variable damping.

Based on the equivalent model, the dynamic equation of the powertrain system can be obtained as shown in Equation (1). When $K_d = 0$ and $C_d = 0$, the equation is the differential equation of the currently common automobile powertrain system.

$$J\{\ddot{\theta}\} + K\{\theta\} + K_g\{\theta_g\} = \{T\} \tag{1}$$

$$J = \begin{pmatrix} J_1 \\ J_2 \\ J_3 \\ \vdots \\ J_{17} \end{pmatrix}, \{\theta\} = \begin{pmatrix} \theta_1 \\ \theta_2 \\ \theta_3 \\ \vdots \\ \theta_{17} \end{pmatrix}, K_g = \begin{pmatrix} 0 & 0 \\ \vdots & \vdots \\ C_d & K_d \\ \vdots & \vdots \\ 0 & 0 \end{pmatrix} \begin{matrix} \left.\vphantom{\begin{matrix}0\\0\\0\end{matrix}}\right\}11 \\ \\ \left.\vphantom{\begin{matrix}0\\0\end{matrix}}\right\}5 \end{matrix},$$

$$\{\theta_g\} = \begin{pmatrix} \dot{\theta}_{12} - \dot{\theta}_d \\ \theta_{12} - \theta_d \end{pmatrix}, T = \begin{pmatrix} 0 \\ T_{total} \\ T_{total} \\ T_{total} \\ T_{total} \\ 0 \\ \vdots \\ 0 \\ T_f \\ 0 \\ T_f \end{pmatrix}_{17 \times 1}$$

$$K = \begin{pmatrix}
K_1 & -K_1 & 0 & 0 & 0 & 0 & 0 & 0 & 0 & 0 & 0 & 0 & 0 & 0 & 0 & 0 & 0 \\
-K_1 & K_1+K_2 & -K_2 & 0 & 0 & 0 & 0 & 0 & 0 & 0 & 0 & 0 & 0 & 0 & 0 & 0 & 0 \\
0 & -K_2 & K_2+K_3 & -K_2 & 0 & 0 & 0 & 0 & 0 & 0 & 0 & 0 & 0 & 0 & 0 & 0 & 0 \\
0 & 0 & -K_3 & K_3+K_4 & -K_4 & 0 & 0 & 0 & 0 & 0 & 0 & 0 & 0 & 0 & 0 & 0 & 0 \\
0 & 0 & 0 & -K_4 & K_4+K_5 & -K_5 & 0 & 0 & 0 & 0 & 0 & 0 & 0 & 0 & 0 & 0 & 0 \\
0 & 0 & 0 & 0 & -K_5 & K_5+K_6 & -K_6 & 0 & 0 & 0 & 0 & 0 & 0 & 0 & 0 & 0 & 0 \\
0 & 0 & 0 & 0 & 0 & -K_6 & K_6+K_7 & -K_7 & 0 & 0 & 0 & 0 & 0 & 0 & 0 & 0 & 0 \\
0 & 0 & 0 & 0 & 0 & 0 & -K_7 & K_7+K_8 & -K_8 & 0 & 0 & 0 & 0 & 0 & 0 & 0 & 0 \\
0 & 0 & 0 & 0 & 0 & 0 & 0 & -K_8 & K_8+K_9 & -K_9 & 0 & 0 & 0 & 0 & 0 & 0 & 0 \\
0 & 0 & 0 & 0 & 0 & 0 & 0 & 0 & -K_9 & K_9+K_{10} & -K_{10} & 0 & 0 & 0 & 0 & 0 & 0 \\
0 & 0 & 0 & 0 & 0 & 0 & 0 & 0 & 0 & -K_{10} & K_{10}+K_{11} & -K_{11} & 0 & 0 & 0 & 0 & 0 \\
0 & 0 & 0 & 0 & 0 & 0 & 0 & 0 & 0 & 0 & -K_{11} & K_{11}+K_{12} & -K_{12} & 0 & 0 & 0 & 0 \\
0 & 0 & 0 & 0 & 0 & 0 & 0 & 0 & 0 & 0 & 0 & -K_{12} & K_{12}+K_{13}+K_{15} & -K_{13} & 0 & -K_{15} & 0 \\
0 & 0 & 0 & 0 & 0 & 0 & 0 & 0 & 0 & 0 & 0 & 0 & -K_{13} & K_{13}+K_{14} & -K_{14} & 0 & 0 \\
0 & 0 & 0 & 0 & 0 & 0 & 0 & 0 & 0 & 0 & 0 & 0 & 0 & -K_{14} & K_{14} & 0 & 0 \\
0 & 0 & 0 & 0 & 0 & 0 & 0 & 0 & 0 & 0 & 0 & 0 & -K_{15} & 0 & 0 & K_{15}+K_{16} & -K_{16} \\
0 & 0 & 0 & 0 & 0 & 0 & 0 & 0 & 0 & 0 & 0 & 0 & 0 & 0 & 0 & -K_{16} & K_{16}
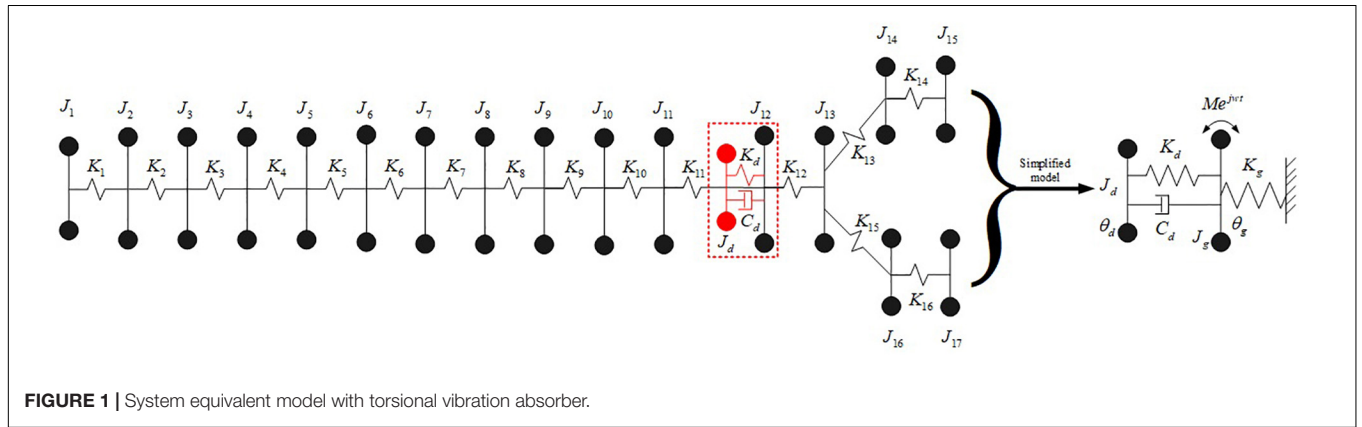\end{pmatrix}$$

FIGURE 1 | System equivalent model with torsional vibration absorber.

The periodic fluctuating torque of the engine is the main excitation source of the powertrain system, including the torque T_g produced by the cylinder gas pressure and the inertial torque T_i of the rotating parts. The formulas of the output torque T_{total} of the engine are as follows (Robert, 2007).

$$T_g = \left(P_A A_g\right) R \sin(\omega t)\left[1 + \frac{R}{l}\cos(\omega t)\right] \quad (2)$$

$$T_i = \frac{1}{2}m_B R^2 \omega^2\left[\frac{R}{2l}\sin(\omega t) - \sin(2\omega t) - \frac{3R}{2l}\sin(3\omega t)\right] \quad (3)$$

$$T_{total} = T_g + T_i \quad (4)$$

The equivalent damping torque of the powertrain system is formulated as follows.

$$T_f = (F_w + F_r)\, r_{wheel}/i_0 \quad (5)$$

$$F_w = \frac{C_D A V^2}{21.15} \quad (6)$$

$$F_r = \chi m_v g \quad (7)$$

TABLE 1 | Natural frequency value and sensitivity analysis.

Order	1th	2th	3th	4th	5th	6th
Natural frequency (Hz)	1.59	6.82	32.06	36.70	64.01	211.03
Sensitivity analysis	J_{16}	J_{15}	J_5	J_{13}	J_{12}	J_8

To solve the inherent characteristics of the powertrain system, the torsional differential equation of the un-damped free vibration of the powertrain system is obtained as follow.

$$J\{\ddot{\theta}\} + K\{\theta\} = \{0\} \quad (8)$$

The natural frequencies and sensitivity analysis of the powertrain system are obtained as shown in **Table 1**.

A four-cylinder four-stroke engine is adopted here. The second-order main harmonic is the main excitation of the engine and the main factor that causes the torsional vibration of the powertrain system. From the following formula, the frequency of the second-order main harmonic of engine excitation can be obtained.

$$f = \frac{r \cdot n_p}{60} \quad (9)$$

Here $r = 2$ is set. It is well known that the rotating velocity range of an automobile engine is generally between 1500 and 6000 rpm. Formula 9 and **Table 1** show that the rotating
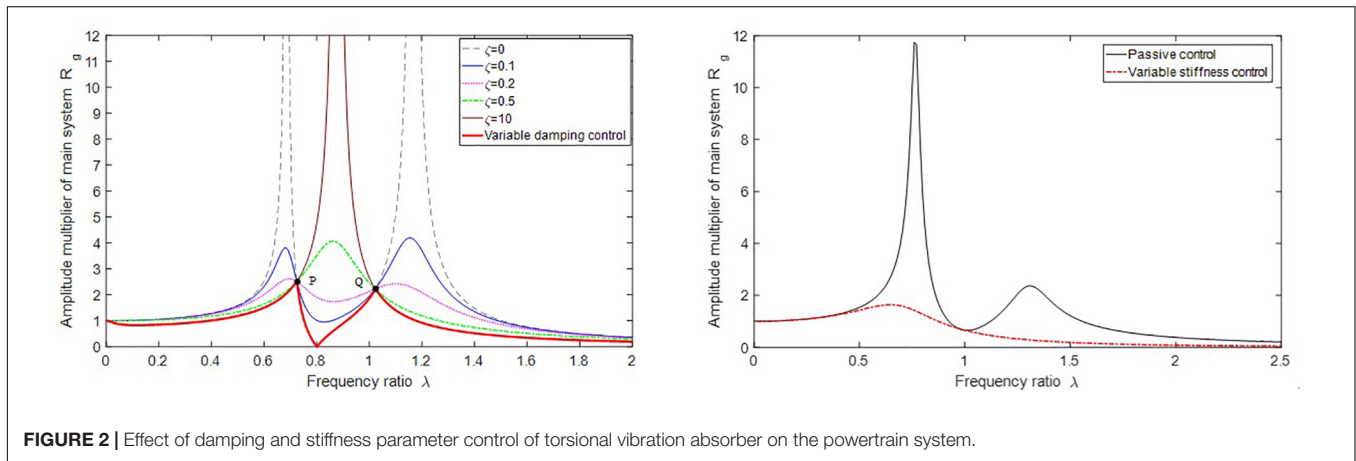
FIGURE 2 | Effect of damping and stiffness parameter control of torsional vibration absorber on the powertrain system.

velocity corresponding to the 5th order natural frequency of the powertrain system is 1920 rpm, which is within the normal working rotating velocity range of the engine. When the engine approaches this rotating velocity, resonance will occur, which will affect the ride comfort of the vehicle, and may cause fatigue damage to the system components. The emphasis of this paper is to effectively suppress the torsional vibration of the powertrain system near to the rotating velocity of 1920 rpm by installing a torsional vibration absorber.

According to the sensitivity analysis of the moment of inertia to the eigenvalues of the system, it can be seen that the moment of inertia of the J_{12} inertia disk is most sensitive to the 5th-order natural frequency of the system, which also determines the installation position of the torsional vibration absorber as shown in **Figure 1**.

To analyze the vibration reduction mechanism of the torsional vibration absorber, a two-degree-of-freedom simplified torsional vibration model is obtained as shown on the right side of **Figure 1** by taking the powertrain system as a whole. The dynamic equation of the two-degree-of-freedom torsional vibration model is as follows.

$$\begin{cases} J_g \ddot{\theta}_g + C_d(\dot{\theta}_g - \dot{\theta}_d) + K_d(\theta_g - \theta_d) + K_g\theta_g = M(t) \\ J_d \ddot{\theta}_d - C_d(\dot{\theta}_g - \dot{\theta}_d) - K_d(\theta_g - \theta_d) = 0 \end{cases} \quad (10)$$

Take the excitation torque as $M(t) = Me^{jwt}$. Assume that the solution to equation (10) is as follows.

$$\theta_g = A_g e^{i\omega t} \theta_d = A_d e^{i\omega t} \quad (11)$$

Then the amplitude of the main system can be obtained.

$$A_g = \frac{M(K_d - J_d\omega^2 + iC_d\omega)}{[(K_g - J_g\omega^2)(K_d - J_d\omega^2) - J_d K_d\omega^2] + iC_d\omega(K_g - J_g\omega^2 - J_d\omega^2)} \quad (12)$$

Here we introduce the following parameter variables.

$$\mu = \frac{J_d}{J_g}, \lambda = \frac{\omega}{\omega_g}, \gamma = \frac{\omega_d}{\omega_g}, A_{st} = \frac{M}{K_g}, \zeta = \frac{C_d}{2\sqrt{J_d K_d}}.$$

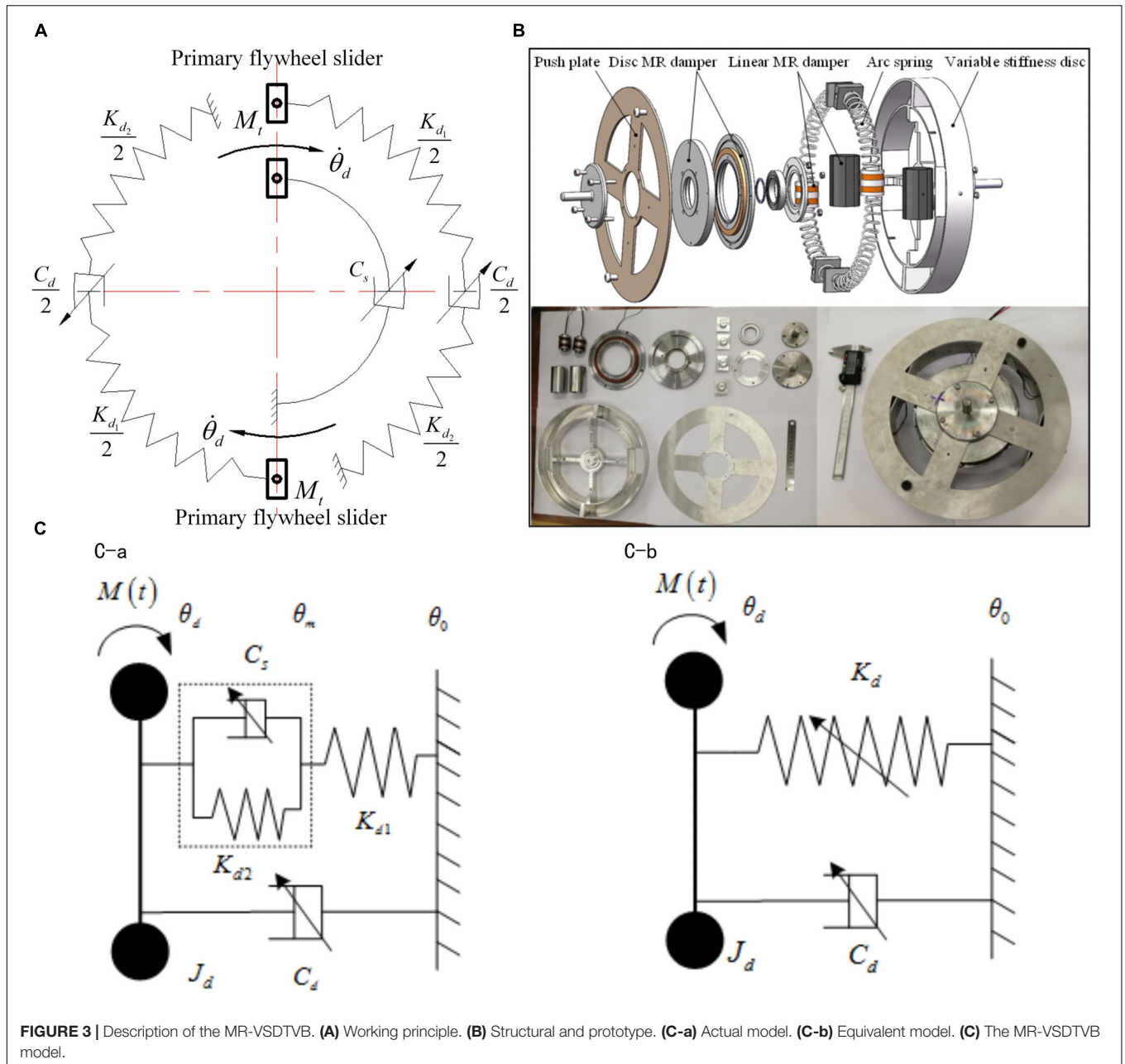TABLE 2 | Equivalent model parameters of the powertrain system.

Number	The moment of inertia $(kg \cdot mm^2)$	Torsional stiffness (Nm/rad)
1	141	20883.49
2	5386	99891.12
3	5512	99891.12
4	5512	99891.12
5	5421	45362.60
6	85200	2109.55
7	1171	3155.81
8	551	89160.87
9	2332	5340.25
10	1592	15831.01
11	2898	28871.35
12	2722	1919.67
13	547	278.06
14	11722	331.63
15	1554162	303.06
16	11722	331.63
17	1554162	

The amplitude multiplier of the main system R_g can be expressed as.

$$R_g = \left| \frac{A_g}{A_{st}} \right| = \sqrt{\frac{(\gamma^2 - \lambda^2)^2 + (2\zeta\lambda)^2}{(2\zeta\lambda)^2(\lambda^2 - 1 + \mu\lambda^2)^2 + [\mu\lambda^2\gamma^2 - (\lambda^2 - 1)(\lambda^2 - \gamma^2)]^2}} \quad (13)$$

As a typical two-degree-of-freedom system, when the absorber's damping ratio ς is changed, the system's amplitude radio curves with different damping ratios can be obtained. When the natural frequency ratio of torsional vibration absorber to the main system $\gamma = 1$ is set, the passive control curve in the right picture of **Figure 2** can be obtained. The following results can be obtained by introducing $f = \frac{\omega}{\omega_d}$ into Equation (13).

$$R_g = \left| \frac{A_g}{A_{st}} \right| = \sqrt{\frac{(1 - f^2)^2 + \left(2\zeta\frac{f^2}{\lambda}\right)^2}{\left(2\zeta\frac{f^2}{\lambda}\right)^2(\lambda^2 - 1 + \mu\lambda^2)^2 + [\mu\lambda^2 - (\lambda^2 - 1)(f^2 - 1)]^2}} \quad (14)$$

FIGURE 3 | Description of the MR-VSDTVB. **(A)** Working principle. **(B)** Structural and prototype. **(C-a)** Actual model. **(C-b)** Equivalent model. **(C)** The MR-VSDTVB model.

Where f is the ratio of the excitation frequency to the natural frequency of the torsional vibration absorber. When $f = 1$ is set, it means that the natural frequency of the torsional vibration absorber changes with the change of the excitation frequency. Hence, the variable stiffness control curve in the right picture of **Figure 2** is obtained. It can be seen that the vibration response of the main system can be effectively improved by real-time control of the damping and stiffness of the torsional vibration absorber.

Here the ratio $\mu = \frac{J_d}{J_g}$ is obtained and the equivalent model parameters of the powertrain systerm are shown in **Table 2**. The moment of inertia J_d of the torsional absorber can be selected. Since the required control frequency of the powertrain

system is $f_5 = 64Hz$, the stiffness adjustment range of the MR-VSDTVB needs to cover the stiffness value corresponding to the frequency f_5.

MR VARIABLE STIFFNESS AND DAMPING VIBRATION ABSORBER

Sections 2 verifies that the variable stiffness and damping torsional vibration absorber can effectively suppress the torsional vibration of the main system within a certain frequency range, through changing the stiffness and damping values in real time. A magneto-rheological variable stiffness and damping torsional
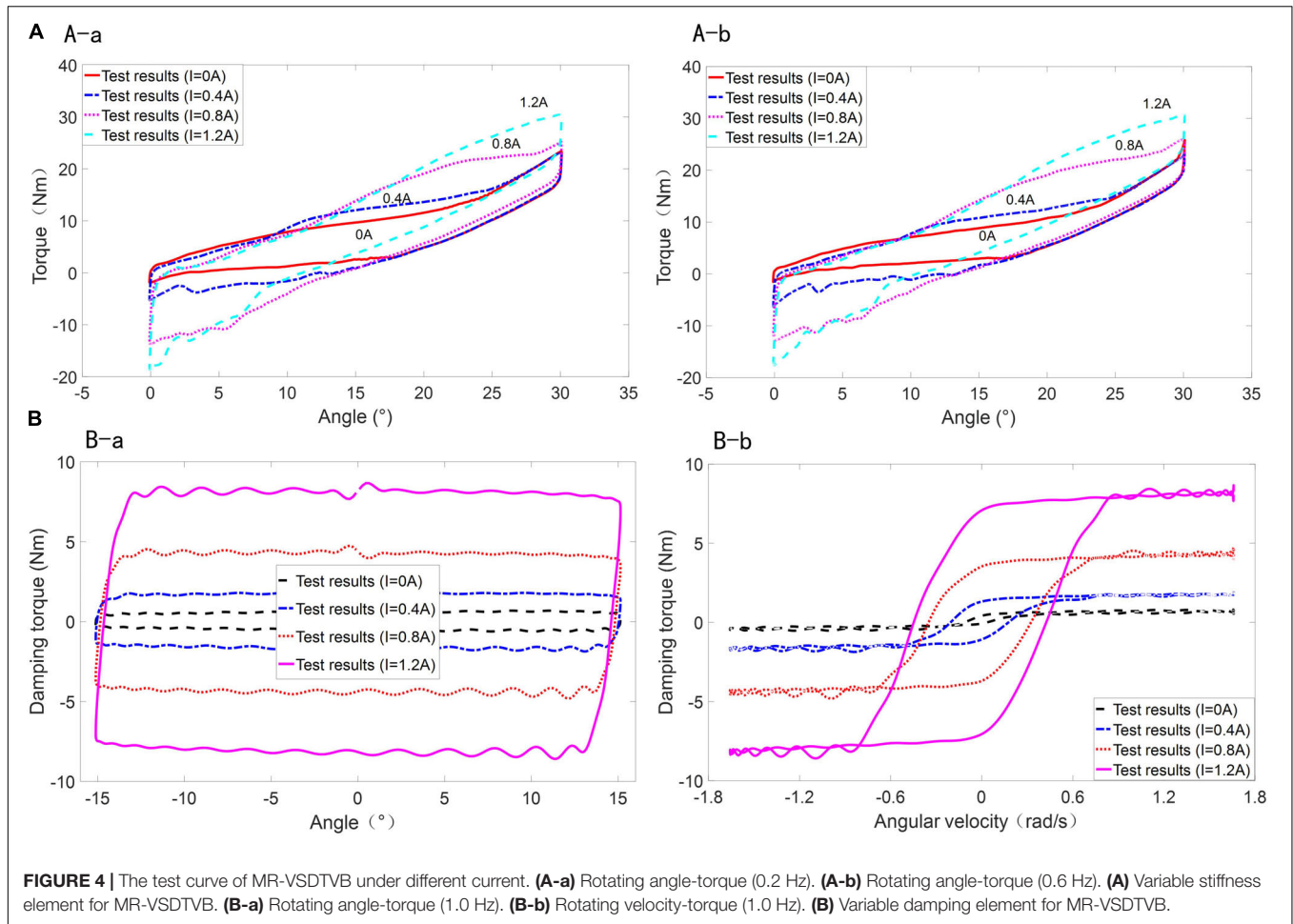
FIGURE 4 | The test curve of MR-VSDTVB under different current. **(A-a)** Rotating angle-torque (0.2 Hz). **(A-b)** Rotating angle-torque (0.6 Hz). **(A)** Variable stiffness element for MR-VSDTVB. **(B-a)** Rotating angle-torque (1.0 Hz). **(B-b)** Rotating velocity-torque (1.0 Hz). **(B)** Variable damping element for MR-VSDTVB.

vibration absorber (MR-VSDTVB) was designed and fabricated to realize the research on torsional vibration control of the powertrain system.

Structure and Working Principle of MR-VSDTVB

Figures 3A,B show that the MR-VSDTVB consists of a rotating variable damping element and a rotating variable stiffness element in parallel. The core component of the rotating variable damping element is a disk MR damper. The rotating variable stiffness element consists of two sets of variable stiffness components which are symmetrically installed in the variable stiffness disc groove. Each set of variable stiffness components involes a linear MR damper and two arc springs with different stiffness, which are placed at both ends of the damper.

When the primary flywheel and the sliders of the MR-VSDTVB rotate under the action of the external torque, the primary and secondary flywheels of the MR-VSDTVB rotate relatively to each other accordingly. In addition, the torque between them is composed of the damping torque generated by variable damping element and the stiffness generated by variable stiffness element. The semi-active adjustment of the damping torque of variable damping element can be achieved

by changing the current applied to the disk MR damper. The stiffness torque generated by variable stiffness element is composed of the damping forces generated by linear MR dampers, and the spring forces generated by compression deformation of the springs K_{d2} and K_{d1}. The damping forces provided by the linear MR dampers can be adjusted by changing the currents applied to coils of the dampers, and compressive deformation of the springs K_{d2} and K_{d1} can be changed, respectively, without changing the total deformation amount. Finally, the purpose of indirectly adjusting the stiffness of variable stiffness element is achieved. The details of the MR-VSDTVB are specified in paper (Wang, 2019), which will not be described here. The MR-VSDTVB model can be obtained from the working principle and structure of the MR-VSDTVB as shown in **Figure 3C**.

Figure 3C-a shows that MR damper C_s is connected in parallel with arc spring K_{d2}, then connected in series with arc spring K_{d1} to form equivalent variable stiffness element, and finally connected in parallel with MR damper C_d to form the MR-VSDTVB. The equations of motion for the system shown in **Figure 3C-a** are as follows.

$$\begin{cases} J_d \cdot \ddot{\theta}_d + C_s \cdot (\dot{\theta}_d - \dot{\theta}_m) + K_{d2} \cdot (\theta_d - \theta_m) + C_d \cdot (\dot{\theta}_d - \dot{\theta}_0) = M(t) \\ K_{d1} \cdot (\theta_m - \theta_0) = C_s \cdot (\dot{\theta}_d - \dot{\theta}_m) + K_{d2} \cdot (\theta_d - \theta_m) \end{cases} \quad (15)$$

TABLE 3 | Parameters of the MR- VSDTVB model.

	Positive rotating velocity				Negative rotating velocity		
d_0	2.38	e_0	−5.58	d_0	9.89	e_0	−17.64
g_0	−6.18	h_0	−0.22	g_0	−6.62	h_0	−0.66
d_1	−2.69	e_1	6.30	d_1	15.11	e_1	−27.41
g_1	3.14	h_1	1.98	g_1	12.46	h_1	−0.33
d_2	0.29	e_2	−0.70	d_2	−3.21	e_2	6.41
g_2	−1.37	h_2	−0.31	g_2	−3.13	h_2	0.39
d_3	3.78e-2	e_3	−7.74e-2	d_3	0.25	e_3	−0.56
g_3	0.24	h_3	3.09e-2	g_3	0.31	h_3	−0.07
d_4	−7.19e-3	e_4	1.44e-2	d_4	−9.63e-3	e_4	2.37e-2
g_4	−1.79e-2	h_4	−1.66e-3	g_4	−1.53e-2	h_4	4.9e-3
d_5	3.29e-4	e_5	−6.4e-4	d_5	1.82e-4	e_5	−5.1e-4
g_5	5.8e-4	h_5	4.43e-5	g_5	3.71-4	h_5	−1.6e-4
d_6	−4.65e-6	e_6	8.91e-6	d_6	−1.41e-6	e_6	4.55e-6
g_6	−6.82e-6	h_6	−4.39e-7	g_6	−3.62e-6	h_6	1.83e-6
b_1	1.75	b_2	−6.4	b_3	3.28	b_4	0.09
b_5	−0.29	b_6	0.15	b_7	10.23	b_8	0.65
b_9	−12.22	b_{10}	28.82	b_{11}	−2.26	b_{12}	−3.73
b_{13}	9.61	b_{14}	−3.13	f_0	0.27		

Let the excitation torsion torque $M(t) = M_0 e^{iwt}$, $\theta_0 = 0$, and it can be obtained from the upper equations.

$$\frac{\Theta_d}{M_0} = \frac{1}{-J_d \cdot \omega^2 + K_{d1} - (K_{d1}^2 \cdot (K_{d1} + K_{d2})/(K_{d1} + K_{d2})^2 + C_s^2 \cdot \omega^2) \atop + i \cdot (C_d + (K_{d1}^2 \cdot C_s/(K_{d1} + K_{d2})^2 + C_s^2 \cdot \omega^2)) \cdot \omega}$$

(16)

The corresponding transfer function of the equivalent model shown in **Figure 3C-b** is

$$\frac{\Theta_d}{M_0} = \frac{1}{-J_d \cdot \omega^2 + K_d + i \cdot C_d \cdot \omega}$$

(17)

Comparing Equation (17) with Equation (16), the equivalent stiffness and damping coefficients are as follows.

$$K_d = K_{d1} - \frac{K_{d1}^2 \cdot (K_{d1} + K_{d2})}{(K_{d1} + K_{d2})^2 + C_s^2 \cdot \omega^2}$$

$$= K_{d1} \cdot \left[1 - \frac{1 + \eta}{(1 + \eta)^2 + \left(\frac{C_s \cdot \omega}{K_{d1}}\right)^2} \right]$$

(18)

$$C_d' = C_d + \frac{K_{d1}^2 \cdot C_s}{(K_{d1} + K_{d2})^2 + C_s^2 \cdot \omega^2} = C_d + \frac{1}{\frac{(1+\eta)^2}{C_s} + C_s \cdot \left(\frac{\omega}{K_{d1}}\right)^2}$$

(19)

Where $\eta = \frac{K_{d2}}{K_{d1}}$. Equations (18) and (19) indicate that equivalent stiffness K_d is only related to C_s, and C_d' is influenced by C_s and C_d. If $C_s = 0$, the n$K_d = K_{d1} \cdot K_{d2}/(K_{d1} + K_{d2})$, $C_d' = C_d$. If $C_s = \infty$, then $K_d = K_{d1}$, $C_d' = C_d$. Hence, adjusting the damping coefficient C_s can play an equivalent role in regulating the stiffness of the system. Although adjusting the damping coefficients C_s and C_d can adjust the equivalent damping C_d' of the system, the effect of damping C_d on the equivalent damping of the system is much greater than that of damping C_s. Consequently, two MR dampers C_s and C_d with controllable damping coefficients can be used to adjust the equivalent damping and stiffness of the system approximately independently.

Control Modeling of MR-VSDTVB

Considering that the variable stiffness element and variable damping element of MR-VSDTVB are arranged in parallel, the test scheme adopted here is to test the mechanical characteristics of the two elements separately. The performances of MR-VSDTVB under different excitation frequencies, different excitation angular amplitudes, and different currents were tested on the MTS test bench. The stiffness and damping mechanical properties of MR-VSDTVB were tested, respectively, and the test curves of **Figures 4A,B** are selected as representative for display.

Figure 4A shows that the torque required by MR-VSDTVB at the same rotation angle increases with the increase of current, which also indicates that the stiffness of MR-VSDTVB increases gradually.

It can be seen from **Figure 4B-a** that under the same amplitude and frequency conditions, the damping force of MR-VSDTVB also increases continuously with the increment of current, so is the envelope of the power diagram. Consequently, the energy consumption of MR-VSDTVB increases with the increase of current. From **Figure 4B-b**, it is known that the damping torque of MR-VSDTVB increases with the increment of the current at the same rotation velocity.

Figures 4A,B show that the stiffness force and damping force of MR-VSDTVB have a controllable characteristic. The semi-active control of the stiffness and damping of the MR-VSDTVB can be achieved indirectly by controlling the coil currents.

According to the characteristic analysis of the test curves of the MR-VSDTVB's variable stiffness element and variable damping element, it is found that the polynomial model is suitable for the modeling of the variable stiffness element T_d, and the hyperbolic tangent model is suitable for the modeling of the variable damping element T_c. The mathematical expressions of the hyperbolic tangent model and polynomial model are as follows.

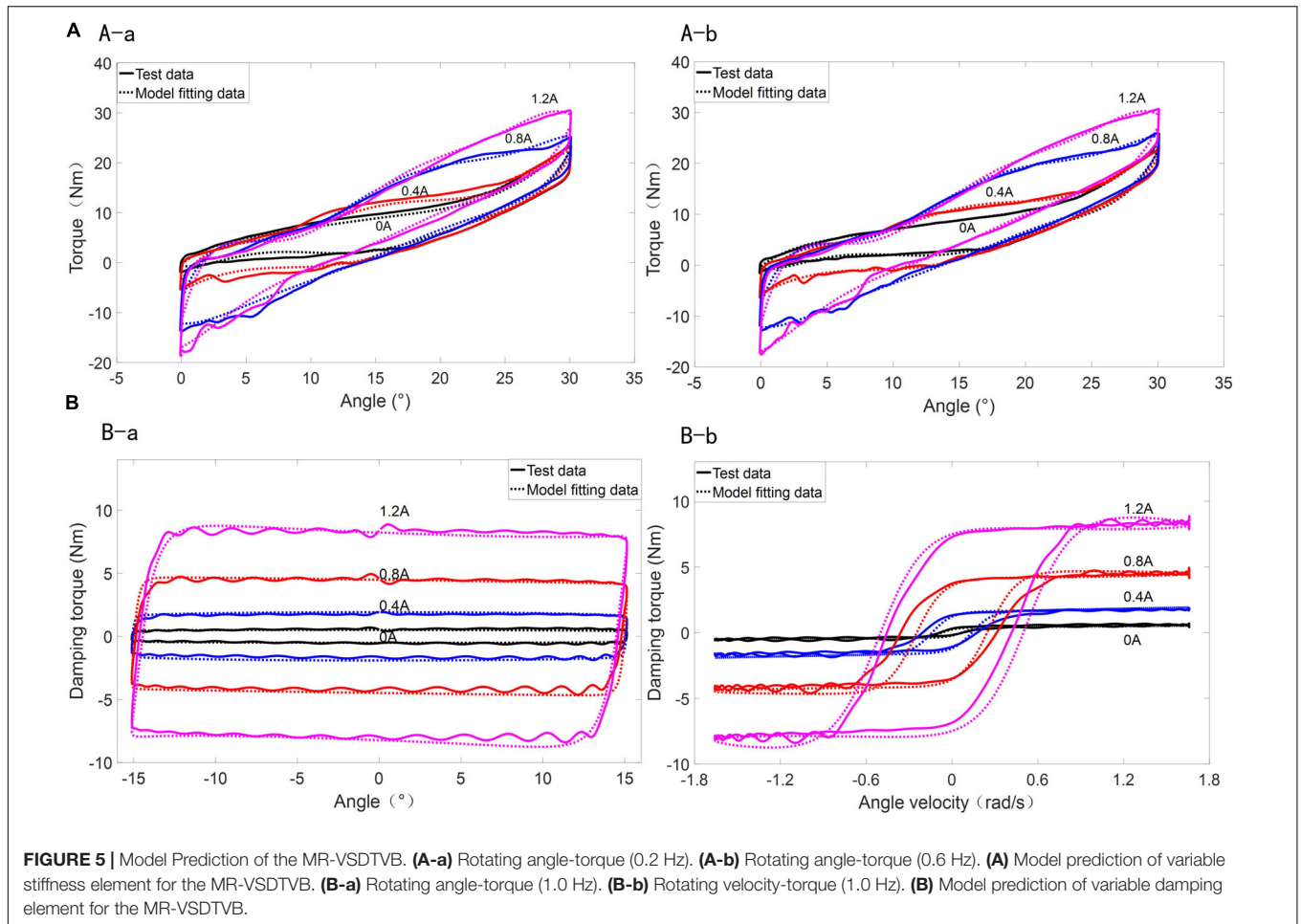$$T_c = c \cdot \omega + k \cdot \theta + \alpha \tanh(\beta \cdot \omega + \delta sign(\theta)) + f_0$$

(20)

$$T_d = \sum_i^n a_i \omega^i$$

(21)

Where $c = b_1 I^2 + b_2 I + b_3$, $k = b_4 I^2 + b_5 I + b_6$, $\alpha = b_7 I + b_8$, $\beta = b_9 I^2 + b_{10} I + b_{11}$, $\delta = b_{12} I^2 + b_{13} I + b_{14}$, $a_i = d_i I^3 + e_i I^2 + g_i I + h_i$ and I is the applied current input.

By fitting the test data with the above mathematical models, the parameters of the mathematical models are obtained as shown in **Table 3**.

Equations (20) and (21) may be expressed as.

$$\min \xi_1(I) = abs \left\{ \begin{array}{c} T_c - (b_1 I^2 + b_2 I + b_3) \cdot \omega + (b_4 I^2 + b_5 I + b_6) \cdot \theta \\ + (b_7 I^2 + b_8 I + b_9) \tanh((b_{10} I + b_{11}) \cdot \omega \\ + (b_{12} I + b_{13}) sign(\theta)) + f_0 \\ s.t. \ 0 \le I \le 2 \end{array} \right\}$$

(22)

FIGURE 5 | Model Prediction of the MR-VSDTVB. **(A-a)** Rotating angle-torque (0.2 Hz). **(A-b)** Rotating angle-torque (0.6 Hz). **(A)** Model prediction of variable stiffness element for the MR-VSDTVB. **(B-a)** Rotating angle-torque (1.0 Hz). **(B-b)** Rotating velocity-torque (1.0 Hz). **(B)** Model prediction of variable damping element for the MR-VSDTVB.

$$\begin{cases} \min \xi_2(I) = abs \left\{ T_d - \sum_i^n (g_i I + h_i)\omega^i \right\} \\ s.t. \quad 0 \leq I \leq 2 \end{cases} \quad (23)$$

For functions (22) and (23), the optimization method, such as the Golden Section method, can be used to obtain the required control currents of the variable stiffness element and the variable damping element (Aliases are the inverse models), respectively. In the actual system test, the look-up table method can be used to ensure the response speed of the real-time control.

$$I_c = \min \xi_1^{-1}(I) \quad (24)$$

$$I_d = \min \xi_2^{-1}(I) \quad (25)$$

The control currents of the variable damping element I_c and the variable stiffness element I_d are used for semi-active control of the MR-VSDTVB's damping torque and stiffness torque, respectively.

The polynomial model of the variable stiffness element and hyperbolic tangent model of the variable damping element are compared with the test data of MR-VSDTVB as shown in **Figures 5A,B**.

Figures 5A,B show that the mathematical models used here can approximate the test data well and describe the hysteresis characteristics of MR-VSDTVB under the illustrated frequency and amplitude as well as different currents. Similar results are also found at other excitation frequencies and amplitudes. **Figure 5** also shows that when the torque of the variable stiffness element of MR-VSDTVB is known at any relative angle, the corresponding stiffness can be obtained, which reveals the stiffness and the torque are both controllable and available in real time.

HUMAN-SIMULATED INTELLIGENT CONTROL (HSIC) ALGORITHM OF THE POWERTRAIN SYSTEM WITH MR-VSDTVB

The Origin of HSIC Algorithm

To effectively suppress the torsional vibration of the powertrain system, a human-simulated intelligent controller (HSIC) is designed. The original HSIC algorithm, which was first proposed by Zhou and Bai (1983) in 1983, has become a fundamental and systematic method used in resolving some general industrial
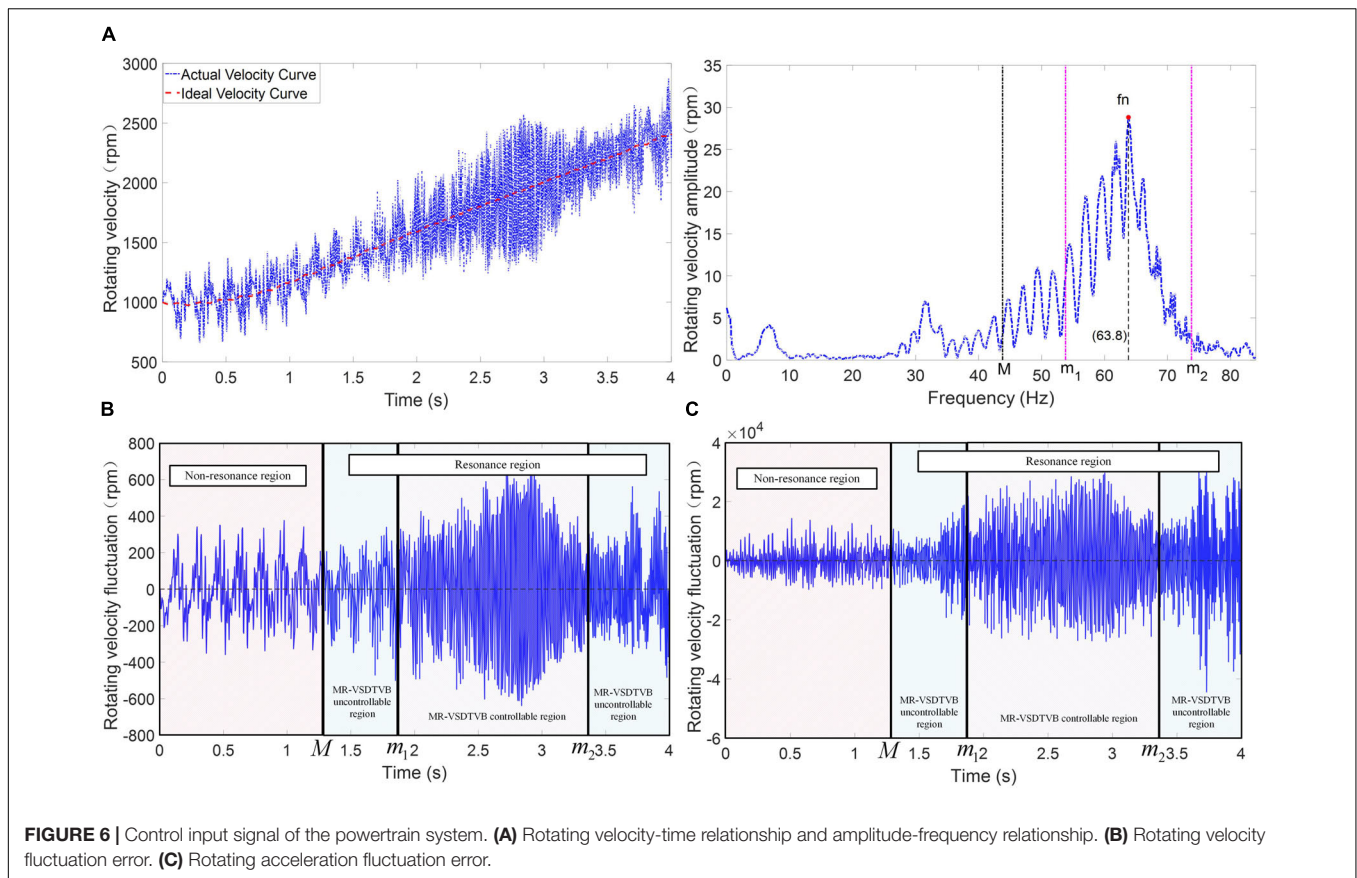
FIGURE 6 | Control input signal of the powertrain system. **(A)** Rotating velocity-time relationship and amplitude-frequency relationship. **(B)** Rotating velocity fluctuation error. **(C)** Rotating acceleration fluctuation error.

control problems for the last 30 years. In recent years, the HSIC theory has been further advanced through combing with the schema theory of modern cognitive science. After many years of research, HSIC theory based on sensory-motor intelligent schema (SMIS) has come into being (Li et al., 2004). The theory provides a more effective and systematic method in resolving some complex control problems.

Design of HSIC Controller

By setting the engine cylinder pressure in the time domain, the ideal rotating velocity of the main reducer's shaft is obtained from the design of the test plan. In the numerical simulation process, the ideal rotating velocity of the main reducer's shaft is obtained through the transmission ratio of the powertrain system. The input shaft of the main reducer actual rotating velocity-time relationship and ideal rotating velocity-time relationship are shown in **Figure 6A**. In the process of acceleration, the difference between the actual rotating velocity curve and the ideal rotating velocity curve are selected as the rotating velocity fluctuation error. The photograph on the right side of **Figure 6A** is the amplitude-frequency curve, which is obtained by Fourier transforming of the rotating velocity curve of the main reducer's input shaft.
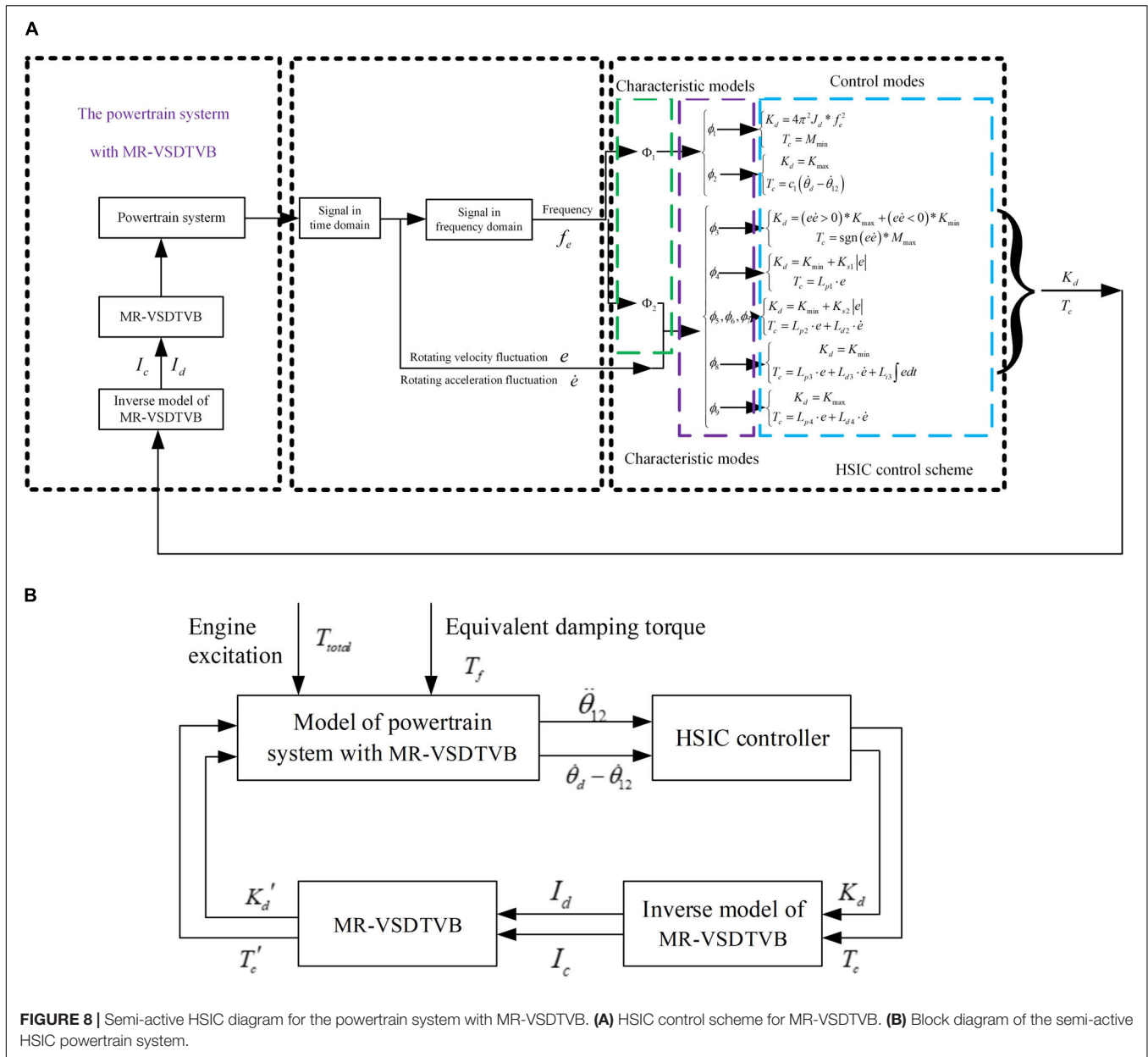
The system excitation main frequency f_e, the rotating velocity fluctuation error and the rotating acceleration fluctuation error

(error e and error derivative $\dot{e}$) of the main reducer's input shaft are selected as input signals as shown in **Figure 6**. The excitation frequency f_e is used to judge the state of the system. The resonance frequency f_n of the powertrain system, which is shown in the photograph on the right side of **Figure 6A**, is basically consistent with the 5th natural frequency of the powertrain system shown in **Table 1**. The photograph on the right side of **Figure 6A** shows that the region near the resonance frequency f_n is set as the resonance region, and the remaining region is set as non-resonant region. The second section shows that the torsional vibration of the system in the resonance region can be suppressed to a large extent by adjusting the MR-VSDTVB stiffness to make the natural frequency consistent with the excitation frequency of the powertrain system. Because the natural frequency adjustment of the MR-VSDTVB does not cover the entire resonance region in the design and test of the MR-VSDTVB, the resonance region is divided into the MR-VSDTVB controllable region and the MR-VSDTVB uncontrollable region in the actual control as shown in **Figure 6**. The controller divides the state characteristic information space of the system into the following three regions according to **Figure 6**.

$$\begin{cases} \text{Resonant and MR−}VSDTVB \text{ controllable region}: & m_1 \le f_e \le m_2 \\ \text{Resonant and MR−}VSDTVB \text{ uncontrollable region}: \\ & -M \le f_e \le m_1 \, or \, m_2 \le f_e \le M \\ \text{Non − resonant region}: & |f_e - f_n| > M \end{cases} \quad (26)$$
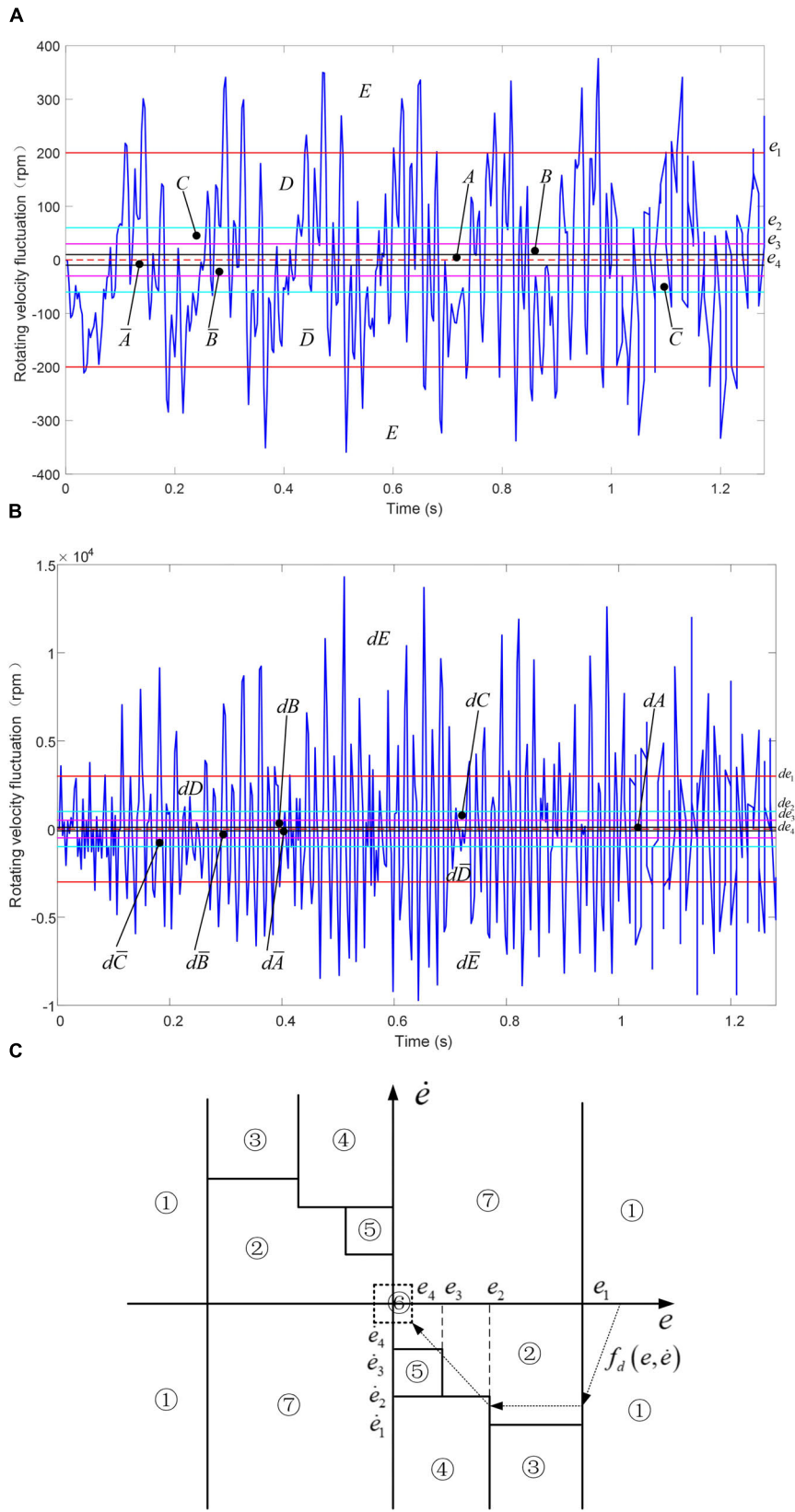
FIGURE 7 | Error Classification of HSIC. **(A)** Rotating velocity fluctuation error in non-resonant region. **(B)** Rotating acceleration fluctuation error in non-resonant region. **(C)** Feature model of HSIC.
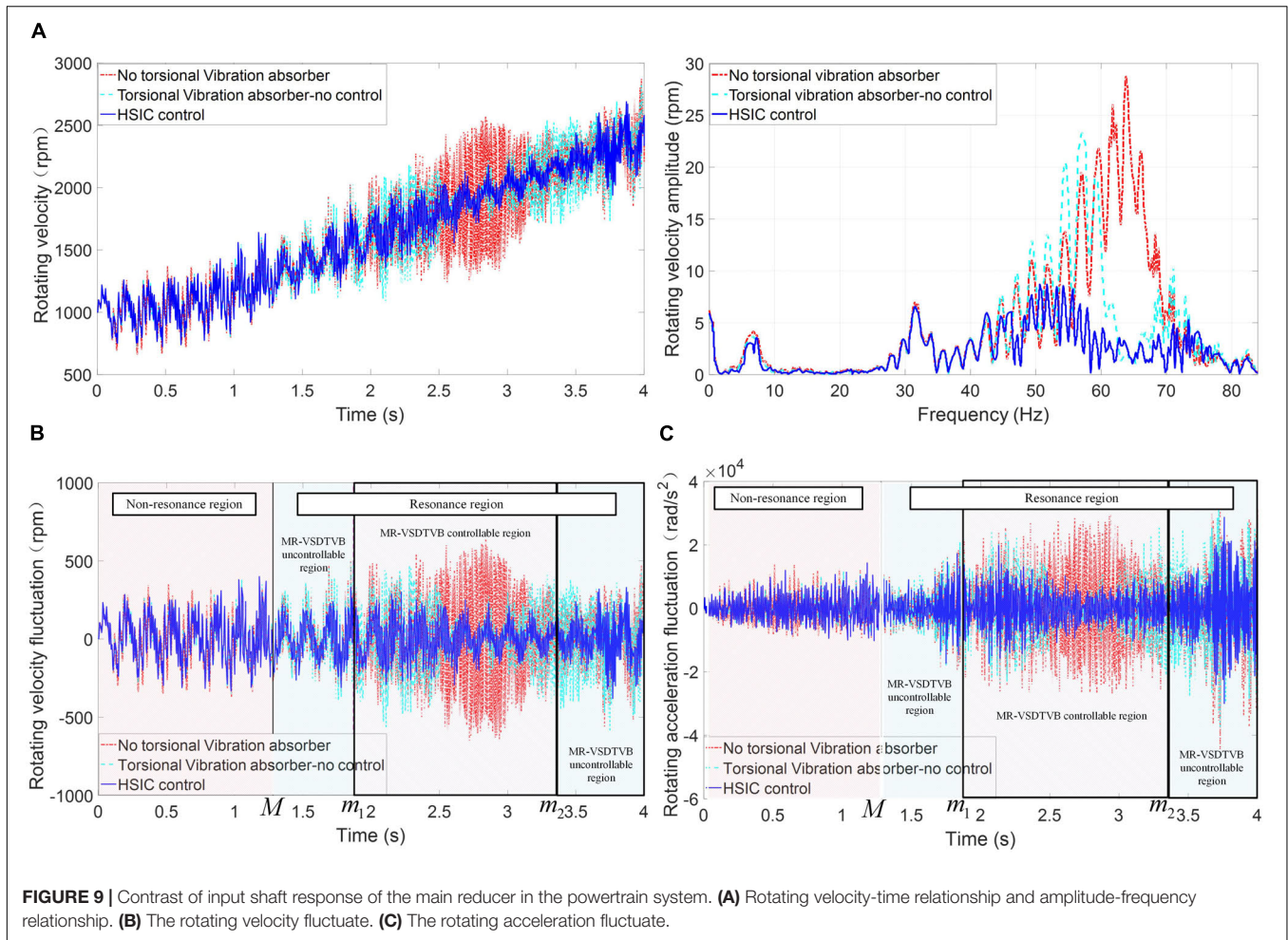
FIGURE 8 | Semi-active HSIC diagram for the powertrain system with MR-VSDTVB. **(A)** HSIC control scheme for MR-VSDTVB. **(B)** Block diagram of the semi-active HSIC powertrain system.

Where f_n represents the 5th natural frequency of the powertrain system, which is approximately 64 Hz. M denotes the range of the resonance region. $M = 20$ is adopted according to the description of **Figure 6**. $[m_1 m_2]$ represents the operating frequency range of MR-VSDTVB.

For the non-resonant region as shown in **Figures 7A,B**, four thresholds e_1, e_2, e_3 and e_4 are set to divide the rotating velocity fluctuation error curve into $A - \bar{A}$, $B - \bar{B}$, $C - \bar{C}$, $D - \bar{D}$, and $E - \bar{E}$ regions according to fluctuation error value. Similarly, four thresholds de_1, de_2, de_3 and de_4 are set to divide the rotating acceleration fluctuation error curve into $dA - d\bar{A}$, $dB - d\bar{B}$, $dC - d\bar{C}$, $dD - d\bar{D}$ and $dE - d\bar{E}$ regions. Different control parameters and control strategies are selected to control the

torsional vibration of the system under different combinations of rotating velocity fluctuation region and rotating acceleration fluctuation region.

Feature model of HSIC in non-resonant region is shown in **Figure 7C**. The abscissa is represented by the rotating velocity fluctuation e, and the ordinate is represented by the rotating acceleration fluctuation e. **Figure 7C** shows that the whole region is transformed into seven characteristic modes, and the dotted lines indicate the desired phase trajectory $f_d (e, \dot{e})$.

The ideal objective for controlling the error trajectory is to make the rotating velocity fluctuation error and the rotating acceleration fluctuation error both reach zero, and the actual

FIGURE 9 | Contrast of input shaft response of the main reducer in the powertrain system. **(A)** Rotating velocity-time relationship and amplitude-frequency relationship. **(B)** The rotating velocity fluctuate. **(C)** The rotating acceleration fluctuate.

rotating velocity follows the ideal rotating velocity of the shaft of the main reducer as shown in **Figure 6A**. When there are errors in the system response, the error trajectory is adjusted along the phase trajectory curve in **Figure 7C** from the larger error regions to the smaller error regions, and finally the desired minimum errors are expected.

Sensed Schema

A sensed schema group can be formulated by:

$$S_p = <R_s, Q, K, \otimes, \Phi>$$

The characteristic primitive set is chosen according to the states of the powertrain system, which can be expressed as follow.

$$Q_1 = \{q_1, q_2\}, Q_2 = \{q_3, q_4, q_5, q_6, q_7, q_8, q_9, q_{10}, q_{11}\}$$

in which $q_1 : |f_e - f_n| \leq M$, $q_2 : m_1 \leq f_e \leq m_2$, $q_3 : e^* \dot{e} \leq 0$, $q_4 : |e| \geq e_1$, $q_5 : |e| \geq e_2$, $q_6 : |e| \geq e_3$, $q_7 : |e| \geq e_4$, $q_8 : |\dot{e}| \geq \dot{e}_4$, $q_9 : |\dot{e}| \geq \dot{e}_3$, $q_{10} : |\dot{e}| \geq \dot{e}_2$, $q_{11} : |\dot{e}| \geq \dot{e}_1$.

The sensed characteristic model can be written as follows, and the characteristic modes are represented by ϕ_i.

$$\Phi_1 = \begin{Bmatrix} \phi_1 \\ \phi_2 \end{Bmatrix} = K_1 \otimes Q_1^T = \begin{Bmatrix} q_2 \\ q_1 \cap \bar{q}_2 \end{Bmatrix}$$

$$\Phi_2 = \begin{Bmatrix} \phi_3 \\ \phi_4 \\ \phi_5 \\ \phi_6 \\ \phi_7 \\ \phi_8 \\ \phi_9 \end{Bmatrix} = K_2 \otimes Q_2^T = \begin{Bmatrix} q_4 \\ q_3 \cap \begin{pmatrix} (\bar{q}_7 \cap q_8 \cap \bar{q}_9) \cup (\bar{q}_6 \cap q_7 \cap \bar{q}_9) \\ \cup (\bar{q}_5 \cap q_6 \cap \bar{q}_{10}) \cup (\bar{q}_4 \cap q_5 \cap \bar{q}_{11}) \end{pmatrix} \\ q_3 \cap \bar{q}_4 \cap q_5 \cap q_{11} \\ q_3 \cap \bar{q}_5 \cap q_{10} \\ q_3 \cap \bar{q}_6 \cap q_9 \cap \bar{q}_{10} \\ \bar{q}_7 \cap \bar{q}_8 \\ \bar{q}_3 \cap \bar{q}_4 \end{Bmatrix}$$
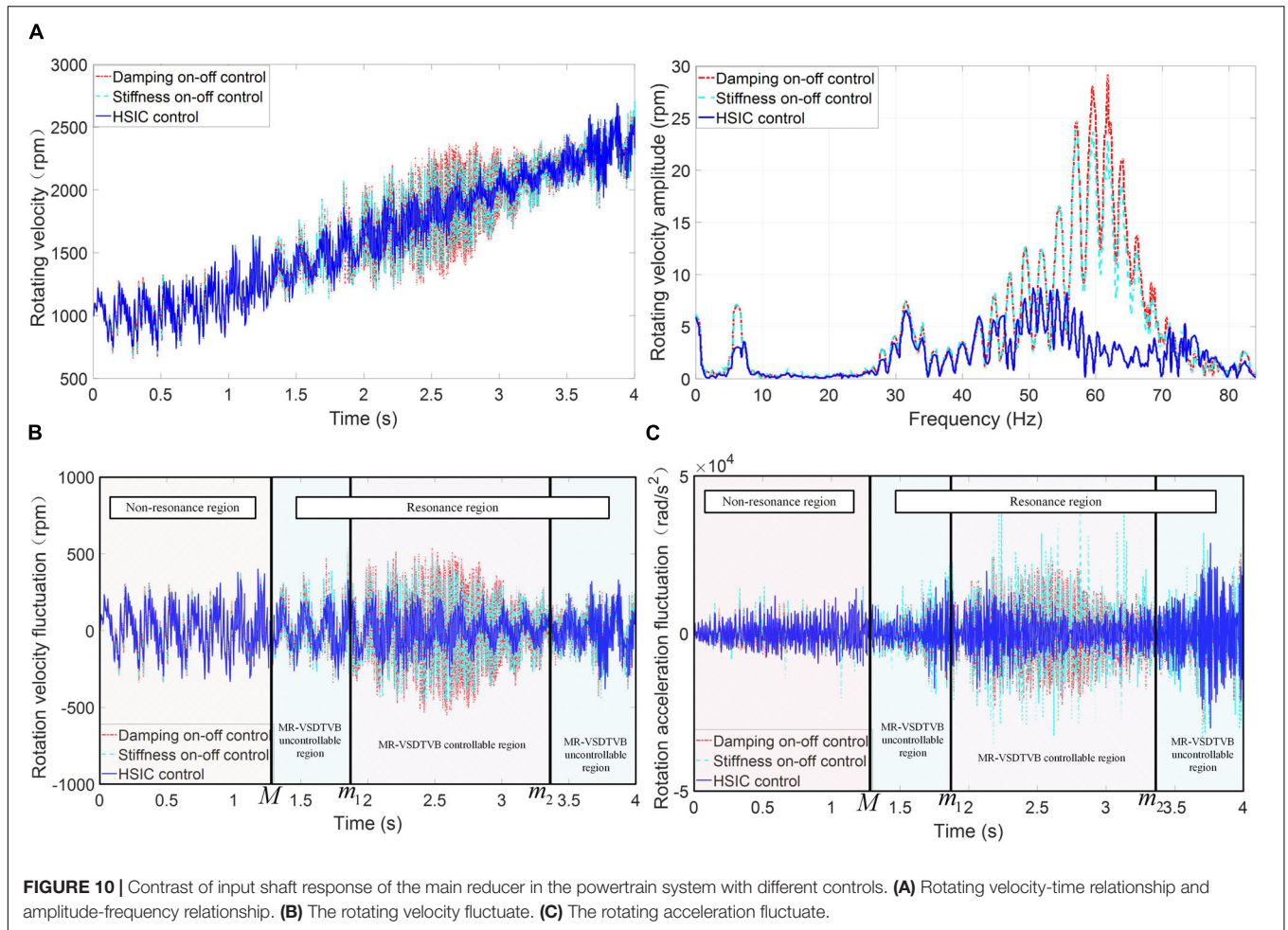
Motion Schema and Association Schema

The motion schema can be described as follow.

$$S_M = <R_s, P, L, \Psi, U>$$

The associated schema can be expressed as follow.

$$\Omega = \{w_1, w_2, w_3, w_4, w_5, w_6, w_7\}$$

FIGURE 10 | Contrast of input shaft response of the main reducer in the powertrain system with different controls. **(A)** Rotating velocity-time relationship and amplitude-frequency relationship. **(B)** The rotating velocity fluctuate. **(C)** The rotating acceleration fluctuate.

where

$$w_1 : \phi_1 \Rightarrow \psi_1 w_2 : \phi_2 \Rightarrow \psi_2 w_3 : \phi_3 \Rightarrow \psi_3 w_4 : \phi_4 \Rightarrow \psi_4$$

$$w_5 : \phi_5 \cup \phi_6 \cup \phi_7 \Rightarrow \psi_5 w_6 : \phi_8 \Rightarrow \psi_6 w_7 : \phi_9 \Rightarrow \psi_7.$$

Figure 8A shows the operation process of the HSIC control scheme of MR-VSDTVB and the relationship between different schemes. According to the measured rotating velocity of the shaft of the main reducer, the corresponding excitation frequency f_e is obtained by Equation (9). When the excitation frequency is in the resonance region, it is necessary to further distinguish whether the excitation frequency is in the MR-VSDTVB controllable region or MR-VSDTVB uncontrollable region, and then the required MR-VSDTVB stiffness value K_d and damping torque value T_c can be obtained through corresponding control modes. When the excitation frequency f_e is in the non-resonant region, the characteristic mode of the current system response is judged by **Figure 7**, and then the required MR-VSDTVB stiffness value K_d and damping torque value T_c can be obtained according to the corresponding relationship between the characteristic modes and the control modes. Further, the control current I_c applied to the variable damping element and I_d applied to the variable stiffness element can be obtained from the inverse model Equation (19)

and (20) of the MR-VSDTVB. Finally, the obtained control currents I_d and I_c are, respectively, applied to the variable stiffness element and the variable damping element of the MR-VSDTVB to realize the semi-active control of the MR-VSDTVB. **Figure 8B** shows the block diagram of the semi-active HSIC powertrain system obtained from **Figure 8A**.

Due to the limitation of the stiffness adjustment range of the MR-VSDTVB and the fact that the damping element of the MR-VSDTVB is an energy dissipating element, the control output is adjusted as follows.

$$K'_d = \begin{cases} K_{\max} & K_d > K_{\max} \\ K_d & K_{\min} < K_d < K_{\max} \\ K_{\min} & K_d < K_{\min} \end{cases}$$

$$T_{MR} = \begin{cases} T_{\max} & T_c \left(\dot{\theta}_d - \dot{\theta}_{12} \right) < 0 \, and \, T_c > T_{\max} \\ T_c & T_c \left(\dot{\theta}_d - \dot{\theta}_{12} \right) < 0 \, and \, T_{\min} < T_d < T_{\max} \\ T_{\min} & Others \end{cases}$$

Where K'_d and T_{MR} represent the actual output stiffness value and damping torque value of the MR-VSDTVB $K_{\max}$ and $K_{\min}$ are the maximum and minimum stiffness values that the MR-VSDTVB
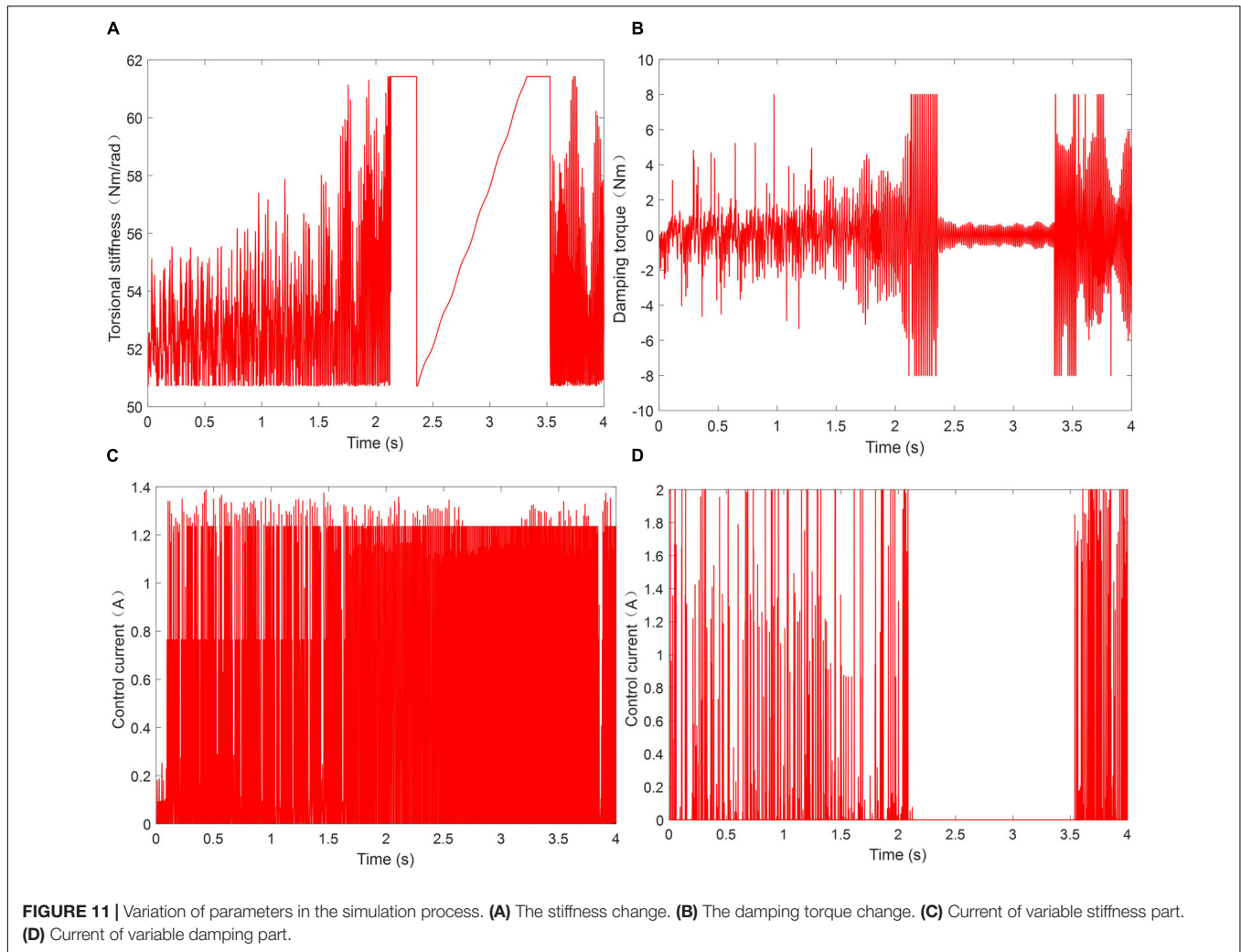
FIGURE 11 | Variation of parameters in the simulation process. **(A)** The stiffness change. **(B)** The damping torque change. **(C)** Current of variable stiffness part. **(D)** Current of variable damping part.

can provide,respectively $\dot{\theta}_d$ and $\dot{\theta}_{12}$ indicate the rotating velocity of the MR-VSDTVB and the main reducer's shaft. T_{max} and T_{min} are the maximum and minimum damping torque values that the MR-VSDTVB can provide.

SIMULATION RESULTS AND DISCUSSION

To verify the effectiveness of the proposed semi-active HSIC controller, a numerical simulation system based on MATLAB/Simulink is established.

In this paper, the torsional vibration response of the main reducer in the powertrain system is taken as the control objective, and the RMS value and the decreasing index of the torsional vibration response are taken as the criteria for evaluating the control effectiveness (Wang et al., 2015). The numerical simulation condition is the acceleration process of the automobile engine from idle condition (900 rpm) to 2500 rpm.

The torsional vibration responses of the input shaft of the main reducer in the powertrain system are compared in three cases, which are without MR-VSDTVB, MR-VSDTVB without control and MR-VSDTVB with control. **Figure 9** shows the numerical simulation results.

The simulation results show that the amplitude of the rotating velocity fluctuation and the rotating acceleration responses can be reduced by installing MR-VSDTVB on the input shaft of the main reducer, and the semi-active HSIC control of MR-VSDTVB can suppress the torsional vibration of the powertrain system to a large extent.
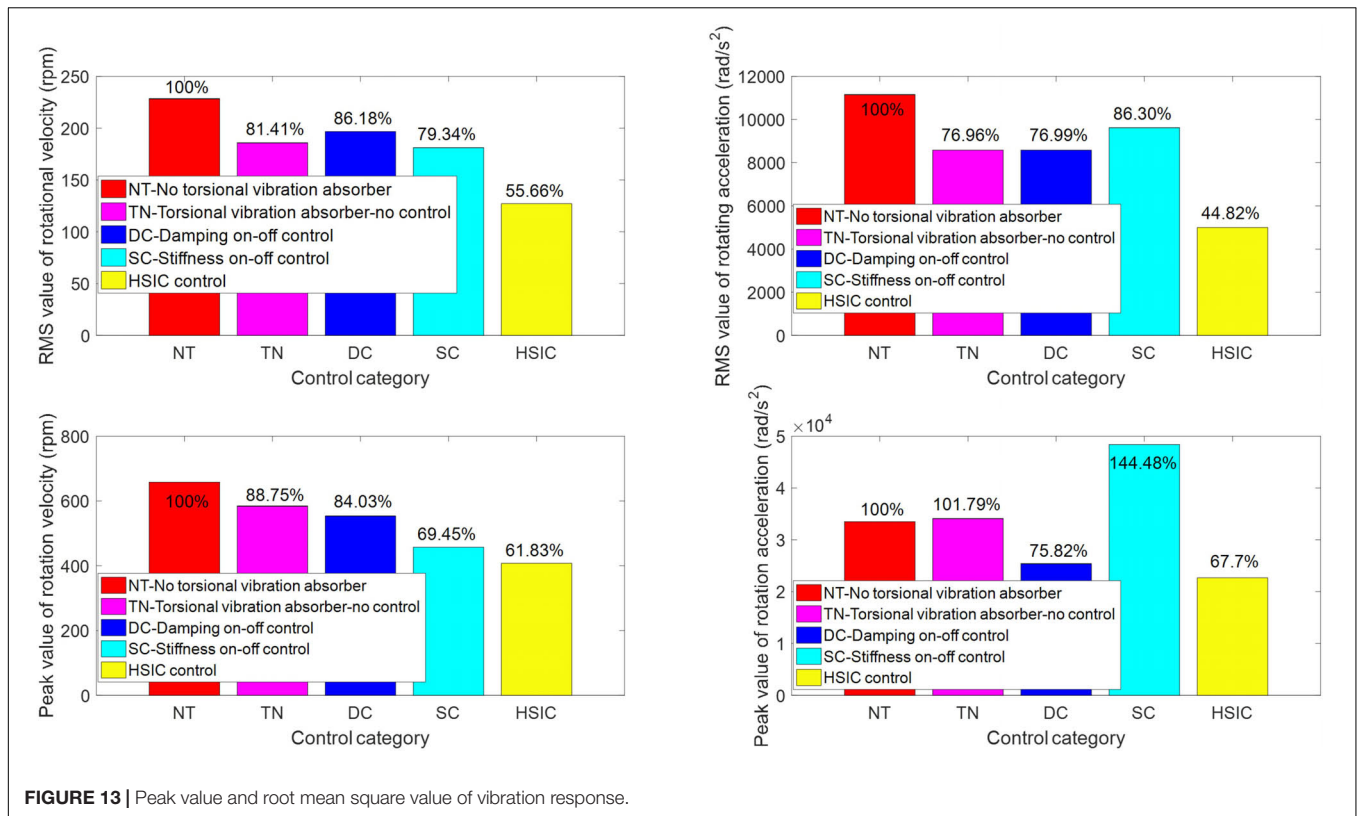
To further verify the control effect of HSIC, the on-off damping control and the on-off stiffness control are adopted for comparison. The expressions of the on-off damping control and the on-off stiffness control are as follows.

$$\begin{cases} c = c_{max} & if \ e\dot{e} \geq 0 \\ c = c_{min} & if \ e\dot{e} < 0 \end{cases}$$

$$\begin{cases} k = k_{max} \ and \ c = c_{max} & if \ e\dot{e} \geq 0 \\ k = k_{min} \ and \ c = c_{min} & if \ e\dot{e} < 0 \end{cases}$$
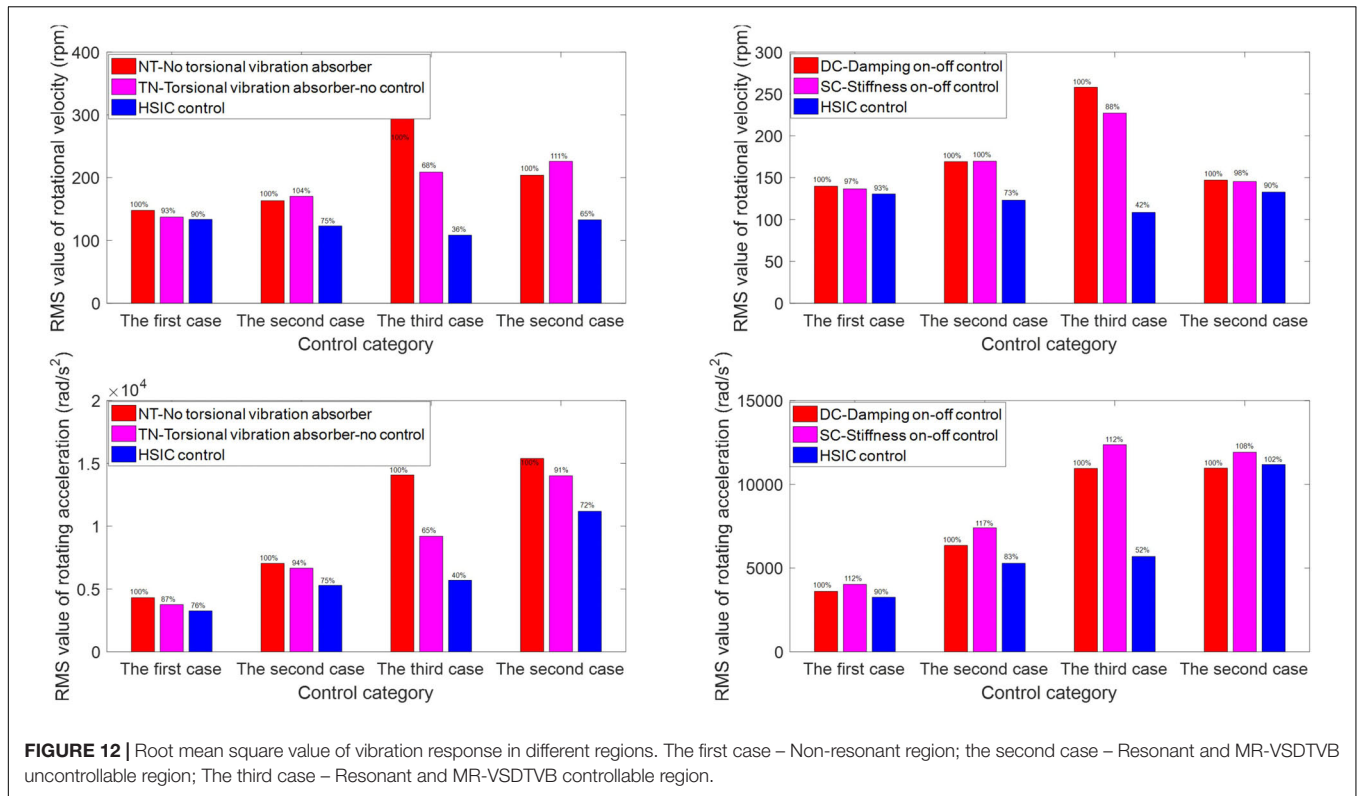
FIGURE 12 | Root mean square value of vibration response in different regions. The first case – Non-resonant region; the second case – Resonant and MR-VSDTVB uncontrollable region; The third case – Resonant and MR-VSDTVB controllable region.

FIGURE 13 | Peak value and root mean square value of vibration response.

The output responses of the powertrain system under different controls are shown in **Figure 10**. **Figure 10** demonstrates that the torsional vibration control effect of HSIC is obviously better than the on-off damping control and the on-off stiffness-damping control, and HSIC can effectively suppress the rotating velocity fluctuation amplitude and rotating acceleration amplitude of the main reducer's input shaft, when the excitation frequency approaches the resonance frequency. The rotating acceleration curve of the on-off stiffness control contains some abrupt amplitudes, which are mainly caused by the step change of stiffness in the control process.

The stiffness change curve and damping torque change curve in the HSIC control process are shown in **Figure 11**, from which the control output under different system responses can be observed. The root mean square values of system responses under different controls in different regions are shown in **Figure 12**, respectively. **Figure 12** shows that HSIC in resonant and MR-VSDTVB controllable region has the excellent torsional vibration control effect, which is obviously better than that in MR-VSDTVB uncontrollable region and non-resonance region. It also shows that a better vibration control effect can be achieved, by adopting the variable stiffness control strategy to make the natural frequency of MR-VSDTVB consistent with the excitation frequency of the system in the resonance region (the RMS values of rotating velocity can be reduced to 36% at most.). The HSIC control in the non-resonance region can also suppress the torsional vibration of the system to a certain degree, and the RMS values of the rotating velocity and the rotating acceleration can be reduced to 90 and 74% at most, respectively.

Based on the above simulation results, the overall peak and RMS values of rotating velocity fluctuation and rotating acceleration of the main reducer's input shaft under different controls are calculated as shown in **Figure 13**. In view of the overall effect of torsional vibration suppression, the peak and RMS values of rotating acceleration can be reduced by 55.18 and 32.3%, respectively, when the HSIC control is applied to MR-VSDTVB. Even the on-off stiffness control and the on-off damping control can effectively reduce the peak and RMS values of rotating velocity to a lower level (by 20.66 and 30.55% at most, respectively).

CONCLUSION

In this study, a MR-VSDTVB and a HSIC controller are proposed to suppress the torsional vibration response of the powertrain system. The details can be concluded as follows.

(a) A MR-VSDTVB is designed, fabricated and tested. Based on the test results, the models of the variable stiffness element and variable damping element of the MR-VSDTVB are proposed.

(b) The multi-degree-of-freedom dynamic model of the powertrain system is established, and the installation position

and adjustment range of MR-VSDTVB are determined by system analysis.

(c) A HSIC controller is proposed to control the MR-VSDTVB to suppress the torsional vibration response of the powertrain system.

(d) The performance of the proposed control strategy is evaluated under the acceleration process of the engine. The numerical simulation results indicate that the semi-active control of MR-VSDTVB with the HSIC controller has a better control effect than other controllers. Compared with the case without MR-VSDTVB, the RMS reduction rates of e and $\dot{e}$ in the powertrain system with MR-VSDTVB are 44.34 and 55.18%, respectively. At the same time, the peak values of e and $\dot{e}$ in the powertrain system with MR-VSDTVB are reduced by 38.17 and 32.30%, respectively, compared with the case without MR-VSDTVB. The torsional vibration of the powertrain system can be suppressed in a wide frequency band by installing the MR-VSDTVB at the specified position of the powertrain system.

DATA AVAILABILITY STATEMENT

The raw data supporting the conclusions of this article will be made available by the authors, without undue reservation, to any qualified researcher.

AUTHOR CONTRIBUTIONS

XD contributed to content layout, and the conception and verification of the whole manuscript. WL was responsible for writing the manuscript and the numerical simulation. CP contributed to auxiliary parts of the simulation and data collection. JX was responsible for verifying the manuscript. XW was responsible for designing and providing technical support for the torsional vibration absorber used in the manuscript. JY contributed to the conception and discussion of the overall framework of the manuscript, and helped to determine and discuss the revision scheme for the manuscript. YZ participated in drawing some of the figures in the manuscript and the modification of the manuscript.

FUNDING

REFERENCES

Davis, C. L., Lesieutre, G. A., Dosch, J. J., and Davis, L. P. (1997). A tunable electrically shunted piezoceramic vibration absorber. *Proc. -Int. Soc. Opt. Eng.* 3045, 51–59.

Deng, H. X., and Gong, X. L. (2007). Adaptive tuned vibration absorber based on magnetorheological elastomer. *J. Intell. Mater. Syst. Struc.* 8, 1205–1210.

Fu, J., Li, P., Liao, G., Lai, J., and Yu, M. (2016). Development and dynamic characterization of a mixed mode magnetorheological elastomer isolator. *IEEE Trans. Mag.* 53, 1–4.

Gao, P., Xiang, C., Liu, H., and Zhou, H. (2018). Reducing variable frequency vibrations in a powertrain system with an adaptive tuned vibration absorber group. *J. Sound Vib.* 425, 82–101.

Harris, B. J., Sun, S. S., and Li, W. H. (2017). Improving stability and curving passing performance for railway vehicles with a variable stiffness MRF rubber joint. *Smart Mater. Struc.* 26, 035–055.

Hoang, N. (2011). *An Adaptive Tunable Vibration Absorber Using Magnetorheological Elastomers for Vibration Control of Vehicle Powertrains.* Sydney: University of Technology Sydney, 1–20.

Huang, H., Sun, S. S., Chen, S. M., and Li, W. H. (2019). Numerical and experimental studies on a new variable stiffness and damping magnetorheological fluid damper. *J. Intell. Mater. Syst. Struc.* 30, 1639–1652.

Johann, M. G., Hermann, P., and Karsten, S. (2014). Innovative torsional vibration reduction devices - vehicle-related design and component strength analysis. *SAE Int. J. Passeng. Cars Mech. Syst.* 7, 1392–1403.

Kang, Q., Wu, Y. D., Deng, J. H., and He, S. D. (2014). Study on the application of torsional vibration damper for the drivetrain torsional vibration of a FR car. *Manuf. Autom.* 36, 92–94.

Li, Z. S., Zhang, H., and Wen, Y. L. (2004). "Human simulated intelligent control based on sensory-motor intelligent schemas," in *Proceedings of the 5th World Congress on Intelligent Control and Automation*, Hangzhou: IEEE 3, 2423–2427.

Nagaya, K., Kurusu, A., Ikai, S., and Shitani, Y. (1999). Vibration control of a structure by using a tunable absorber and an optimal vibration absorber under autotuning control. *J. Sound Vib.* 228, 773–792.

Qian, L. J., Xin, F. L., Bai, X. X., and Wereley, N. (2017). M.State observation–based control algorithm for dynamic vibration absorbing systems featuring magnetorheological elastomers: Principle and analysis. *J. Intell. Mater. Syst. Struc.* 28, 2539–2556.

Qing-Hua, Z., Zhi-Yong, C., Wen-Ku, S., Qing-Hua, Z., and Zhi-Yong, C. (2015). Torsional vibration semi-active control of drivetrain based on magneto-rheological fluid dual mass flywheel. *Math. Probl. Eng.* 2015, 1–17.

Robert, L. (2007). *Norton. Design of machinery.* New York, NY: McGraw Hill, 521–561.

Sun, S. S., Yang, J., and Li, W. H. (2016). Development of an isolator working with magnetorheological elastomers and fluids. *Mech. Syst Signal Process.* 83, 371–384.

Wang, D., Yan, B., Wang, D. L., and Wang, Y. W. (2015). Noise control method of interior booming induced by torsional vibration of driveline system. *Noise Vib. Control.* 35, 73–76.

Wang, X. H. (2019). *Principle and Experiment of Variable Stiffness Damping of Magnetorheological Torsional Damper in Power Driveline.* Chongqing: Chongqing University, 21–49.

Wang, Y., and Jing, X. J. (2018). Nonlinear stiffness and dynamical response characteristics of an asymmetric X-shaped structure. *Mecha. Syst. Signal Process.* 125, 142–169.

Williams, K., Chiu, G., and Bernhard, R. (2002). Adaptive-passive absorbers using shape-memory alloys. *J. Sound Vib.* 249, 835–848.

Xu, Z. B. (2010). *Study on Adaptive Tuned Vibration Absorbing Technology.* Hefei: University of Science and Technology of China, 1–10.

Ye, S. C. (2012). *Passive and Semi-Active Torsional Vibration Control.* Tuscaloosa: The University of Alabama, 1–10.

Yu, J. Q., Dong, X. M., Zhang, Z. L., and Chen, P. G. (2018). A novel scissor-type magnetorheological seat suspension system with self-sustainability. *J.Intell. Mater. Sys. Struc.* 30:1045389X1775425.

Zhang, D. (2015). *Optimizing the Parameters of Dynamic Vibration Absorber and Researching on the Active Control.* Xi'an: Changan University, 1–20.

Zhang, X. Z., and Li, W. H. (2009). Adaptive tuned dynamic vibration absorbers working with MR elastomers. *Smart Struct. Syst.* 5, 517–529.

Zhou, Q. J., and Bai, J. K. (1983). "An intelligent controller of novel design," in *Proceedings of Multi-National InstruCion Conference, Part. 1*, (Shanghai: Science Technology Literature Press), 137–149.

APPENDIX

Nomenclature

J_1 The moment of inertia at the free end of the engine, $kg \cdot mm^2$

J_2, J_3, J_4, J_5 The 1~4 moments of inertia of cylinder crank connecting rod group on the engine, $kg \cdot mm^2$

J_6 The moment of inertia of the flywheel and the front of the clutch, $kg \cdot mm^2$

J_7 The moment of inertia of the driven disk of the clutch and the front part of the input shaft of the transmission, $kg \cdot mm^2$

J_8 The moment of inertia of the rear end of the transmission input shaft and the pair of constant meshing gears, $kg \cdot mm^2$

J_9 The moment of inertia of the main and follower gear pairs in each gear position and the front section of the output shaft, $kg \cdot mm^2$

J_{10} The moment of inertia of the rear section of the output shaft and the front section of the transmission shaft, $kg \cdot mm^2$

J_{11} The moment of inertia of the middle section of the output shaft, $kg \cdot mm^2$

J_{12} The moment of inertia of the rear section of the drive shaft and the main reducer's active components, $kg \cdot mm^2$

J_{13} The moment of inertia of the follower of the main reducer, the differential and the front half of the shaft, $kg \cdot mm^2$

J_{14}, J_{16} The moment of inertia of left axle and left wheels, right axle, and right wheels, respectively, $kg \cdot mm^2$

J_{15}, J_{17} Half of the translational mass equivalent moment of inertia of the vehicle body, respectively, $kg \cdot mm^2$

K_1, K_5 The torsional stiffness between the free end of the engine and the crankshaft, between the flywheel and the crankshaft of the engine, Nm/rad

K_2, K_3, K_4 The torsional stiffness of cylinder crank connecting rod group on the engine, respectively, Nm/rad

K_6 The torsional stiffness of the clutch, Nm/rad

K_7, K_8, K_9 The input shaft torsional stiffness, intermediate shaft torsional stiffness and output shaft torsional stiffness of transmission, Nm/rad

K_{10}, K_{11} The torsional stiffness of the front and middle segments of the transmission shaft, Nm/rad

K_{12} The torsional stiffness of the input shaft of the main reducer, Nm/rad

K_{13}, K_{15} The torsional stiffness of the left and right axes, respectively, Nm/rad

K_{14}, K_{16} The equivalent torsional stiffness of the left and right wheels, Nm/rad

P_A The single cylinder gas pressure, N/m^2;

A_g The piston area of the cylinder, m^2;

R, l The crankshaft radius and connecting rod length, m

ω The crankshaft angular velocity, rad/s

m_B The piston equivalent mass, kg

F_w The air resistance, N

F_r The rolling resistance in motion, N

r_{wheel} The wheel radius, m

i_0 The transmission ratio

C_D The air drag coefficient

A The windward area of the vehicle, m^2

V The driving speed of the vehicle, m/s

χ The rolling damping coefficient between wheel and road

m_v The vehicle mass, kg

g The gravity acceleration, m/s^2

T_g The torque produced by the cylinder gas pressure, Nm

T_i The inertial torque of the rotating parts, Nm

T_{total} The output torque of the engine, Nm

r The order of engine excitation

n_p The resonance speed of the system, rpm

R_s, Q, K, $\otimes$, Φ The input information set, the characteristic primitive set, the relation matrix, the operational symbol, and the characteristic model set, respectively

P, L, Ψ, U The control mode primitive set, the coordination relation matrix, the control mode set, and the control output, respectively

M_{min}, M_{max} The minimum and maximum damping torque provided by MR-VSDTVB, respectively, Nm

K_{min}, K_{max} The minimum and maximum stiffness provided by MR-VSDTVB, respectively, Nm/rad

c_{min}, c_{max} The minimum and maximum damping coefficient provided by MR-VSDTVB, respectively, Nms/rad

K_{s1}, K_{s2} The controllable stiffness selected under different control modes respectively, Nm/rad

$L_{p1 \sim p4}, L_{d2 \sim p4}, L_{i3}, c_1$ The control coefficients selected under different control modes, respectively

J_g The moment of inertia of the main system, $kg \cdot mm^2$

K_g The stiffness of the main system, Nm/rad

J_d The moment of inertia of the torsional vibration absorber, $kg \cdot mm^2$

K_d The stiffness of the torsional vibration absorber, Nm/rad

C_d The damping coefficient of the torsional vibration absorber, Nms/rad

θ_g, θ_d The rotation angle of the main system and the rotation angle of the torsional vibration absorber, rad

$M(t)$ The excitation torque, Nm

μ The Inertia ratio of torsional vibration absorber to the main system

λ The frequency ratio of forced vibration

γ The natural frequency ratio of the torsional vibration absorber to the main system

A_{st} The static deformation of the main system

ζ The damping ratio

ω_g The natural frequency of the main system

ω_d The natural frequency of the torsional vibration absorb